© 2014. Published by The Company of Biologists Ltd | Journal of Cell Science (2014) 127, 288–294 doi:10.1242/jcs.142943

SHORT REPORT

Photobleaching imprinting microscopy: seeing clearer and deeper

Liang Gao, Alejandro Garcia-Uribe, Yan Liu, Chiye Li and Lihong V. Wang*

ABSTRACT

We present a generic sub-diffraction-limited imaging method – photobleaching imprinting microscopy (PIM) – for biological fluorescence imaging. A lateral resolution of 110 nm was measured, more than a twofold improvement over the optical diffraction limit. Unlike other super-resolution imaging techniques, PIM does not require complicated illumination modules or specific fluorescent dyes. PIM is expected to facilitate the conversion of super-resolution imaging into a routine lab tool, making it accessible to a much broader biological research community. Moreover, we show that PIM can increase the image contrast of biological tissue, effectively extending the fundamental depth limit of multi-photon fluorescence microscopy.

KEY WORDS: Fluorescence, Microscopy, Photobleaching Super-resolution

INTRODUCTION

Fluorescence microscopy has been extensively used to gain a deeper understanding of cell and tissue biology (Lichtman and Conchello, 2005). Despite widespread applications, fluorescence microscopy faces a fundamental bottleneck in its resolving capability, the optical diffraction limit, which was first stated by Ernst Abbe in 1873. Owing to this limitation, the achievable spatial resolution of conventional fluorescence microscopy is ~250 nm in the lateral direction and ~500 nm in the axial direction. Because many cellular organelles, such as microtubules, actin fibers and ribosomes, are smaller than this, breaking the optical diffraction limit has been the holy grail of light microscopy over the past several decades.

To address this challenge, a wide array of methodologies has been introduced, allowing the fine structure of a biological cell or tissue to be revealed at the super-resolution level. Depending on the conceptual shared thread, super-resolution techniques are normally based on two distinct strategies. One strategy, referred to as probe-based super-resolution, uses the stochastic nature of photoswitchable fluorophores, sequentially switching them on and off so that the signals from individual fluorescent molecules can be recorded consecutively. Merging all of the single-molecule centroid positions acquired by repeated cycles of photo-activation and photo-deactivation yields a final super-resolution image. Representative modalities using this strategy are stochastic optical reconstruction microscopy (STORM) (Rust et al., 2006), photoactivated localization microscopy (PALM) (Betzig et al., 2006; Hess et al., 2006) and photobleaching-based localization microscopy (Burnette et al., 2011; Munck et al., 2012; Simonson et al., 2011). The second strategy, referred to as illumination-based super-resolution, uses non-linear optical approaches to modify and engineer the point spread function (PSF), resulting in a reduced focal spot size at the sample. Within this category, the most important techniques are stimulated emission depletion microscopy (STED) (Klar et al., 2000), structured illumination microscopy (SIM) (Gustafsson, 2000) and saturated structured illumination microscopy (SSIM) (Gustafsson, 2005). Owing to its superior resolving capability, super-resolution imaging now has become an essential tool for examining a wide variety of biological molecules, pathways and dynamics, providing unprecedented resolution at a scale down to tens of nanometers (Hell, 2007).

In spite of their revolutionary impact, most super-resolution techniques rely on specific fluorescent probes, such as PALM/STORM, or require complicated optical illumination modules, such as STED, limiting access by the general research community. To provide a generic method that can be readily implemented on a standard light microscope with conventional fluorescent dyes, here we present photobleaching imprinting microscopy (PIM) for super-resolution fluorescence imaging. Photobleaching is routinely encountered as a nuisance in fluorescence microscopy (Tsien et al., 2006), which is leveraged here. PIM works by first imprinting a structured pattern onto the sample through photobleaching, followed by light interrogation with another focused Gaussian laser beam. The high-order components related to the laser fluence distribution can be extracted simply by a differential operation between two fluorescence intensities along time-lapse fluorescence decay. Using PIM, we demonstrated a lateral resolution of ~110 nm, more than a twofold improvement over the optical diffraction limit.

PIM can also remove the out-of-focus light, enhancing image contrast and enabling deep imaging. In two-photon fluorescence microscopy (TPFM), the in-focus signals are ultimately limited by near-surface fluorescence (Theer and Denk, 2006). Here we show that, at a depth of 300 µm, whereas TPFM showed almost no contrast between the in-focus signals and background, PIM clearly resolved the sample features. Therefore, PIM is expected to effectively extend the fundamental imaging depth limit of optical microscopy for characterization of deep tissues.

Operating principle

The operating principle of PIM is depicted in Fig. 1A–C. Once a fluorophore is excited from the ground state to an excited state, part of the energy is released by radiative decay, emitting fluorescence with an intensity I equal to

$$I = C\mu_a F^n, \quad (1)$$

where C is a constant, μ_a is the absorption coefficient of the fluorophore, F is the laser fluence, and n denotes the number of photons involved in an excitation event.

Department of Biomedical Engineering, Washington University in St Louis, One Brookings Dr., St Louis, MO 63130, USA.

*Author for correspondence (lhwang@wustl.edu)

Received 17 September 2013; Accepted 30 October 2013

Journal of Cell Science

Journal of Cell Science (2014) 127, 288–294 doi:10.1242/jcs.142943

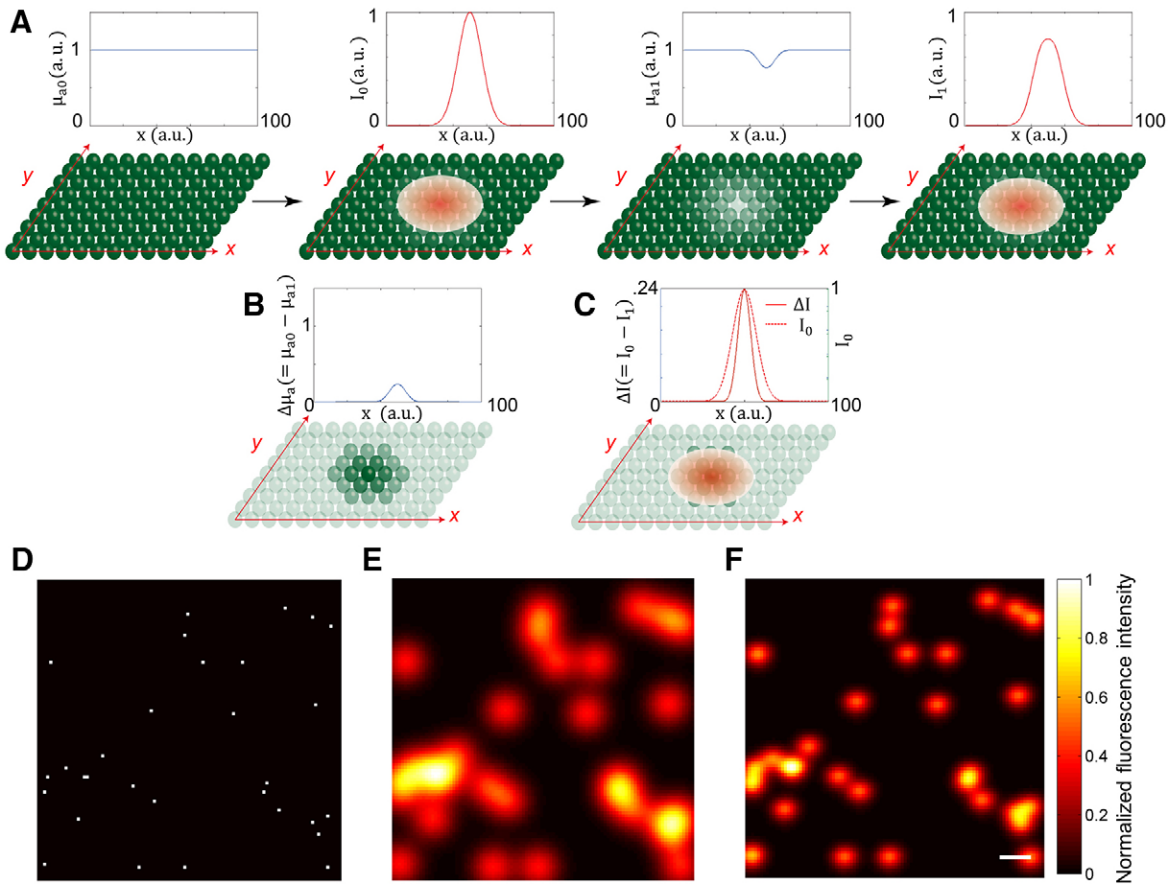

Fig. 1. The operating principle of photobleaching imprinting microscopy (PIM). (A) The fluorophore molecules are first illuminated by a focused Gaussian laser beam, which imprints a photobleaching pattern matching the light intensity distribution. Then the same spot is interrogated by the second focused Gaussian laser beam. (B) The subtraction between the measured fluorescence intensities acquired with these two laser shots yields a differential signal which is proportional to the high order laser fluence distribution. (D–F) Simulation results for confocal fluorescence (E) and PIM (F) imaging of randomly distributed point targets (D). The image has 100×100 pixels, and optical diffraction limited resolution has 10 pixels as indicated by the scale bar. The simulation algorithm is detailed in the Materials and Methods.

In fluorescence microscopy, photobleaching occurs when the excited electrons are trapped in a relatively long-lived triplet state. The forbidden triplet–singlet transition provides the fluorophore with a much longer time to undergo irreversible chemical reactions with the environment than does the singlet–singlet transition (Tsien et al., 2006). The photobleaching of a fluorophore obeys an exponential temporal decay law:

$$\mu_a(t) = \mu_{a0} \exp(-kt), \tag{2}$$

where t is the time, μ_{a0} is the initial absorption coefficient of the fluorophore, and k is the photobleaching rate. The photobleaching rate k is a function of excitation laser fluence F, as described empirically (Patterson and Piston, 2000) as

$$k = BF^m, \tag{3}$$

where B denotes a constant, and m depicts the order of the dependence. For one-photon excitation fluorescence, $m=1$, whereas for two-photon excitation fluorescence, the photobleaching rate increases rapidly with $m \geq 3$ (Patterson and Piston, 2000). Combing Eqs. 1–3 gives

$$I(t) = C\mu_{a0}F^n \exp(-BF^m t). \tag{4}$$

Subtracting the fluorescent intensity measured at a later time t from the initial value measured at $t=0$ pixel by pixel yields a differential image with the following intensity:

$$I_{diff} = C\mu_{a0}F^n[1-\exp(-BF^m t)]. \tag{5}$$

Equation 5 can be further Taylor expanded as

$$I_{diff} = \sum_{l=1}^{\infty} D_l F^{ml+n} = D_1 F^{m+n} + D_2 F^{2m+n} + \cdots. \tag{6}$$

Here $D_l = C\mu_{a0}(-Bt)^l/l!$. In the case of one-photon excitation ($m=1$, $n=1$), the dominating term in Eq. 6 is quadratic, i.e.,

$$I_{diff}^{1P} \propto F^2. \tag{7}$$

In the case of two-photon excitation ($m \geq 3$, $n=2$), the dominating term in Eq. 6 starts with an order K larger than five, i.e.,

$$I_{diff}^{2P} \propto F^K, K \geq 5. \tag{8}$$

The nonlinearity depicted in Eqs 7 and 8 shrinks the PSF in all dimensions, thus enabling super-resolution imaging beyond the

Journal of Cell Science (2014) 127, 288–294 doi:10.1242/jcs.142943

optical diffraction limit as well as super-contrast imaging beyond the conventional depth limit in TPFM.

To show a potential resolution improvement in theory, we simulated a case when a fluorophore, aminocoumarin dextran, was imaged by confocal fluorescence microscopy (CFM) and PIM under two-photon excitation. The original object, the CFM image and the PIM image are shown in Fig. 1D–F, respectively. The simulation algorithm is detailed in Materials and Methods.

RESULTS AND DISCUSSION

Sub-diffraction-limited fluorescence PIM

We first evaluated the lateral resolution of PIM by imaging a sharp edge of a thin fluorescent film (maximal emission wavelength ~520 nm) with a confocal fluorescence microscope. With an oil-immersion objective with a numerical aperture (NA) of 1.4, the full width at half maximum (FWHM) of the PSF measured by PIM was ~110 nm, less than half of the ~280 nm measured by conventional confocal microscopy (Fig. 2A).

Then we imaged a thin layer of aggregated fluorescent microspheres (diameter ~0.9 µm, maximum emission wavelength ~600 nm) sandwiched between two cover glasses. The fluorescent microspheres were excited and photobleached by a He-Ne laser at 543 nm. The pixel dwell time was 200 µseconds, and a total of 200 time-lapse frames were captured. The PIM image intensities were calculated pixel by pixel by a differential operation between two consecutive images and averaged along the fluorescence decay curve (see Materials and Methods). As shown in Fig. 2B, as a result of the crosstalk from adjacent pixels, the contrast in conventional confocal fluorescence images was low. In the corresponding PIM image, owing to the improvement in resolution, the fluorescent microspheres became more distinguishable.

To demonstrate the sub-diffraction-limited imaging capability of PIM in a biological cell, we imaged cellular microtubules (bovine pulmonary artery endothelial cell line) stained with a green fluorescent dye, BODIPY FL Goat Anti-Mouse IgG (F-14781, Life Technologies). The fluorophore was excited and photobleached by an argon laser at 488 nm. Following a similar procedure, 200 time-lapse fluorescence images were measured to extrapolate the PIM image, shown in Fig. 2C. The signal intensities across a line in the zoomed area were plotted and compared between the confocal fluorescence and PIM images (Fig. 2D). Note that at the locations near 4 µm and 6 µm, the microtubules are not discriminable in the confocal fluorescence image, whereas they are well resolved in the corresponding PIM image. In addition, we also imaged cellular mitochondria (NIH 3T3 fibroblast cell line) stained with an orange fluorophore, Mitotracker CMT (M7510, Life Technologies). The sample was excited and photobleached by a He-Ne laser at 543 nm. The acquired confocal fluorescence and PIM images are shown in Fig. 2E. To highlight the difference, a side-by-side image is shown in Fig. 2F. Because PIM relies on fluorescence decay to extract the nonlinear components, we evaluated the gain in

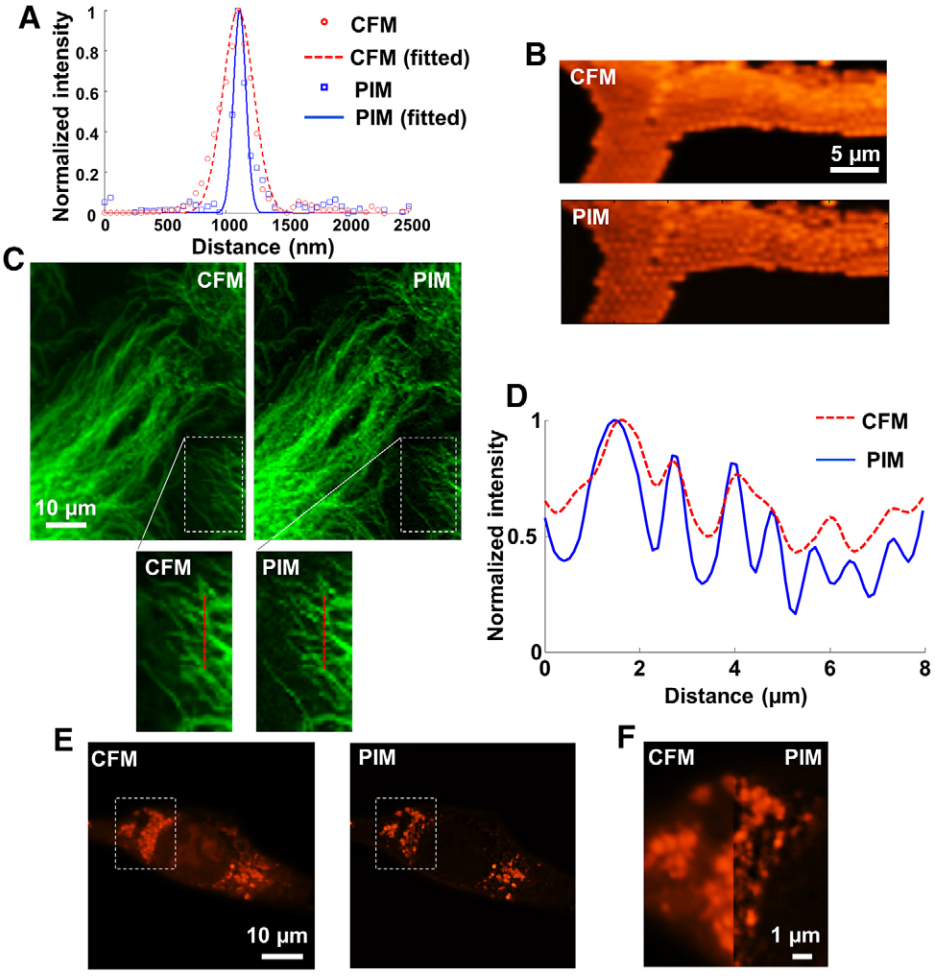

Fig. 2. Sub-diffraction-limited fluorescence imaging by PIM. (A) Comparative measurement of the lateral resolutions of confocal fluorescence microscopy (CFM) and PIM with an oil-immersion microscope objective (NA = 1.4). The fitted PSFs are shown by dashed and solid lines. The full width at half maximum (FWHM) of the CFM PSF is ~280 nm, while that of the PIM PSF is ~110 nm. (B) CFM and PIM images of aggregated fluorescent microspheres. (C) CFM and PIM images of cellular microtubules stained with a green fluorescent dye, BODIPY FL goat anti-mouse IgG. (D) Comparison of fluorescent intensities along the dashed line in the zoomed area in C. (E) CFM and PIM images of cellular mitochondria stained with an orange fluorophore, Mitotracker CMT. (F) Two sub-images from the dashed box in E shown side by side.

Journal of Cell Science (2014) 127, 288–294 doi:10.1242/jcs.142943

resolution improvement against the loss of fluorescence intensity level after the PIM procedure. A measurement showed that the cellular fluorescent intensity was decreased by ~10% owing to photobleaching, indicating the feasibility of multi-cycle PIM imaging before the fluorophore loses its entire fluorescing capability.

Contrast enhancement in multi-color tissue fluorescence imaging by PIM

In CFM, sectioning is achieved by using a pinhole to block the out-of-focus light. However, when the pinhole size is sufficiently small (in practice, smaller than 0.25 Airy unit), the thickness of the optical section is no longer influenced by the pinhole size but solely determined by the axial resolution of the microscope objective in use. By improving the resolution in all dimensions, PIM can reduce the crosstalk from adjacent voxels, thus allowing super-contrast imaging at depths.

To demonstrate the contrast enhancement capability of PIM in tissue fluorescence imaging, we imaged a mouse kidney section (~20 µm thick) stained with a combination of three fluorophores (F24630, Life Technologies). First, the elements of the glomeruli and convoluted tubules were labeled with green fluorescent Alexa Fluor 488. Second, the filamentous actin prevalent in glomeruli and the brush border were stained with red fluorescent Alexa Fluor 568. Third, the nuclei were counterstained with a blue-fluorescent dye, DAPI. The fluorophores were excited at wavelengths of 405 nm, 488 nm and 543 nm. The emitted fluorescence was collected by a microscope objective (NA=1.4) and simultaneously measured in three separate photomultiplier tube (PMT) color channels. An optimal pinhole size was automatically chosen by the microscope to balance the in-focus SNR and optical sectioning. For PIM calculation, a total of 400 time-lapse fluorescence images were captured.

To study the contributions to the PIM image of different order nonlinear components in Eq. 6, we fitted a polynomial function to the measured fluorescent decay pixel by pixel (see Materials and Methods). The images associated with the linear, quadratic and cubic terms of the fluence distribution were extracted and are shown in Fig. 3A, respectively. The green and red fluorescent intensities along the dashed line in the zoomed area were plotted and compared between the linear and nonlinear components (Fig. 3B–E). As expected, a higher-order dependence on the laser fluence led to a higher image contrast.

Extending the fundamental imaging depth limit in two-photon fluorescence microscopy by PIM

Two-photon fluorescence microscopy (TPFM) is an indispensable technique for deep tissue imaging (Helmchen and Denk, 2005; Piston, 1999). As a result of a quadratic dependence on the laser fluence, the excitation in TPFM is spatially confined, enabling intrinsic optical sectioning without a physical pinhole. However, this optical sectioning capability eventually fails at a deeper depth, because the out-of-focus fluorescence gradually overwhelms the in-focus signal in a scattering sample. The depth where the out-of-focus signals are comparable to the in-focus fluorescence is defined as the fundamental imaging depth limit of TPFM (Theer and Denk, 2006).

To demonstrate how the contrast enhancement capability of PIM extends the imaging depth limit in TPFM, we imaged a

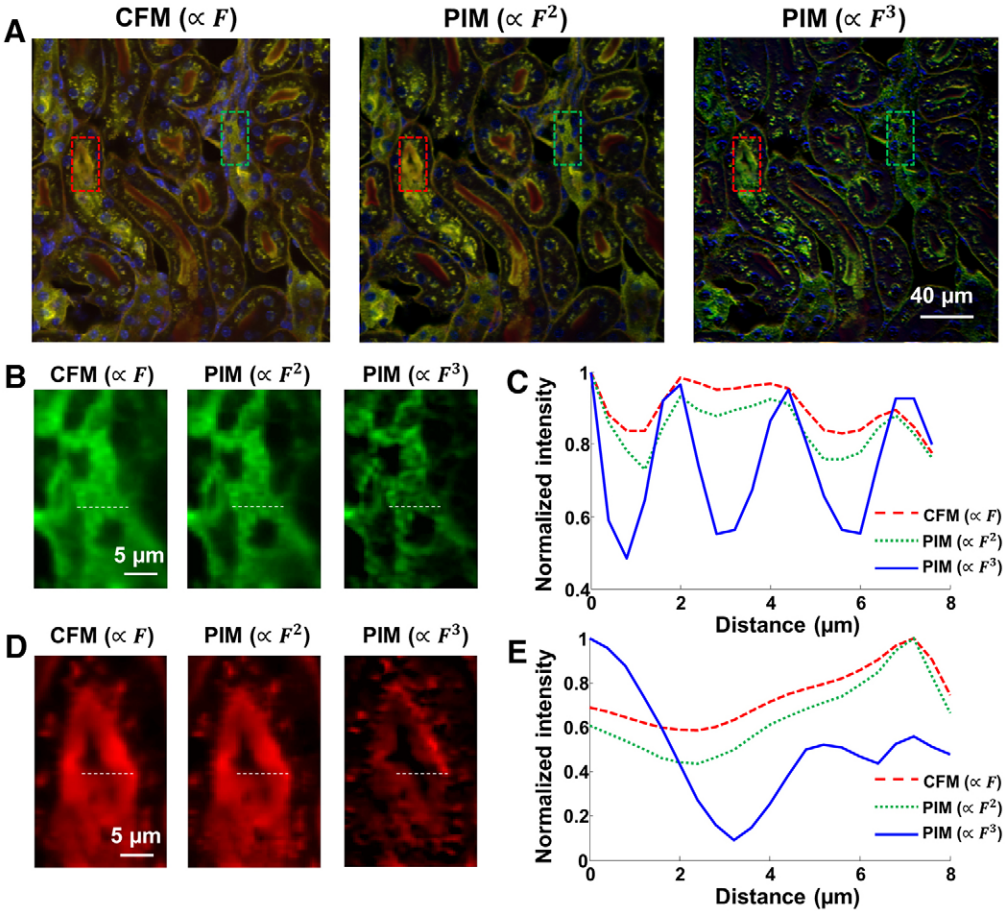

Fig. 3. Contrast enhancement by PIM in multi-color tissue fluorescence imaging. A mouse kidney section was stained with a combination of three fluorophores: (1) The elements of the glomeruli and convoluted tubules were labeled with green-fluorescent Alexa Fluor 488; (2) the filamentous actin prevalent in glomeruli and the brush border were stained with red-fluorescent Alexa Fluor 568; and (3) the nuclei were counterstained with a blue-fluorescent DAPI. (A) Confocal fluorescence microscopy (CFM) image (left), PIM image associated with the quadratic order of laser fluence (middle), and PIM image associated with the cubic order of laser fluence (right). (B) A zoomed area in the green color channel of the CFM and PIM images. (C) Comparisons of signal intensities along the dashed line in B between the CFM and PIM images associated with different orders of the laser fluence distribution. (D) A zoomed area in the red color channel of CFM and PIM images. (E) Comparisons of signal intensities along the dashed line in D between CFM and PIM images associated with different orders of the laser fluence distributions.

Journal of Cell Science (2014) 127, 288–294 doi:10.1242/jcs.142943

phantom consisting of aggregated green fluorescent microspheres covered by a 300 µm thick micro-fiber layer stained with fluorescein. The sample was excited by a Ti-sapphire femtosecond laser at 920 nm, and the two-photon excited fluorescence was collected by a water-immersion objective with an NA of 1.04. To provide a baseline, we first directly imaged the fluorescent microspheres without the scattering layer depicted in Fig. 4A to acquire the reference image shown in Fig. 4B. Then, we covered the sample with the scattering layer (Fig. 4C) and imaged over the same FOV from the top (Fig. 4D). Owing to the fluorescence from the out-of-focus layers, the sample features indicated with an arrow in Fig. 4B are completely obscured in Fig. 4D. Moreover, the fluorescent intensities across the dashed line in Fig. 4D show no contrast between the in-focus signal and background (Fig. 4F). Next, we acquired a PIM image by measuring 400 time-lapse fluorescence images (Fig. 4E). The signal intensities across the same line are shown in Fig. 4F, demonstrating the recovery of the indicated features.

Conclusion

In summary, we present a generic sub-diffraction-limited technique, photobleaching imprinting microscopy, for biological fluorescence imaging. In phantom and cellular imaging experiments, PIM demonstrated over a twofold improvement in resolution. Additionally, we showed that PIM can reduce the out-of-focus light in tissue fluorescence imaging, considerably improving the image contrast. Compared with other super-resolution imaging techniques, PIM is easier to implement on a standard microscope with generic fluorescent dyes, making super-resolution imaging a routine lab technique. It is worth noting that, although techniques such as deconvolution microscopy can also remove image blur, the accuracy is highly dependent on the signal-to-background ratio (Murray, 2011). In particular, the extension of fundamental depth in TPFM as seen in Fig. 4 would not even be possible by solely relying on deconvolution microscopy.

Although not demonstrated here, PIM could also be potentially used in wide-field fluorescence microscopy and light-sheet fluorescence microscopy (LSFM). Owing to a structured fluence distribution along the depth axis, on the one hand, wide-field fluorescence PIM can be used to remove the out-of-focus light, thereby allowing for optical sectioning; on the other hand, light-sheet fluorescence PIM can be exploited to further improve axial resolution, offering a simple solution to a long-standing problem in LSFM on mitigating the trade-off between imaging field-of-view and section thickness (Fahrbach et al., 2013).

The resolution improvement by PIM is achieved at the expense of fluorescence loss. A 10% drop in fluorescence intensity was observed after the PIM procedures. In addition, averaging the differential intensity along the fluorescence decay course is normally required to obtain a sufficient SNR to extrapolate the high-order components, a process that decreases the temporal resolution of the microscope and currently allows monitoring of only slow-varying events. This limitation can be potentially overcome by choosing a smaller FOV, scanning a path of interest with random access, or shortening the pixel dwell time using a higher fluorophore concentration. Moreover, parallel acquisition schemes, such as spinning-disk confocal microscopy, can also be used. Because PIM is based on the photobleaching memory

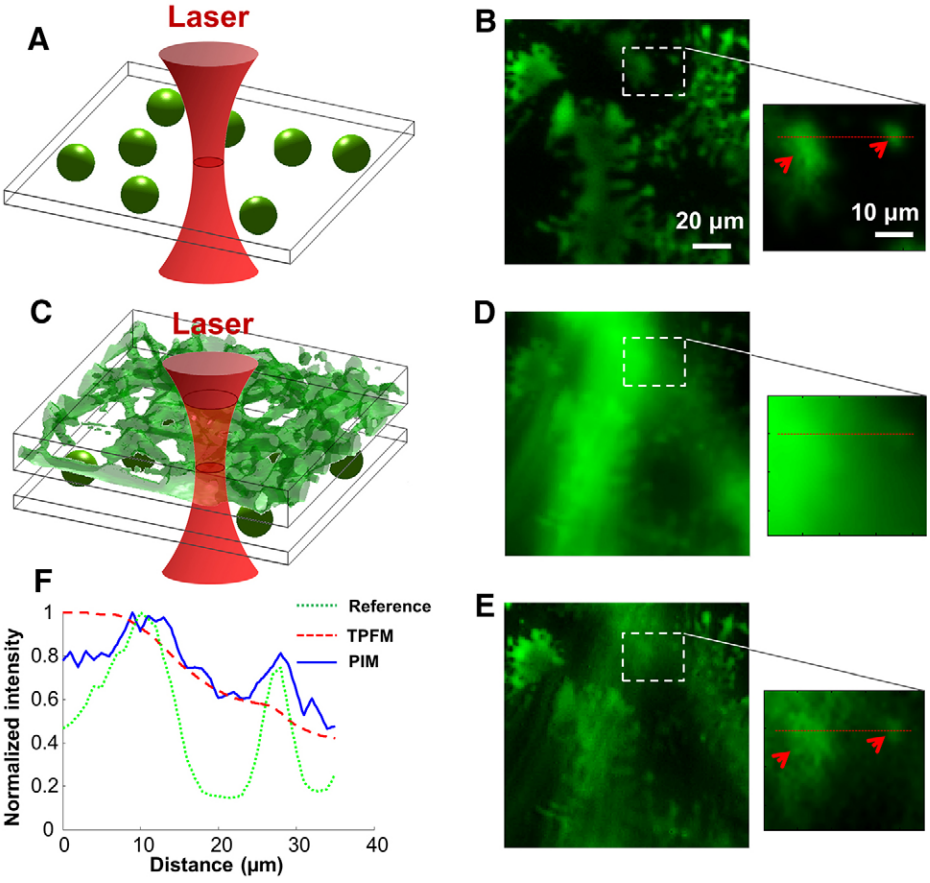

Fig. 4. Extending the fundamental imaging depth limit in two-photon excitation fluorescence microscopy (TPFM) by PIM. (A) Aggregated fluorescent microspheres without the covering scattering layer. (B) TPFM image of the microspheres providing a baseline. (C) To mimic a thick biological tissue, the sample was covered with a heterogeneous scattering layer 300 µm thick. The scattering layer was stained with a green fluorophore, fluorescein. (D) TPFM image of the same field of view as the covering layer. (E) Two-photon PIM image of the same field of view as the covering layer. (F) Comparison of signal intensities along the dashed lines between TPFM and PIM in D and E. The features indicated with an arrow in B are obscured in the TPFM image, but are still discernible in the PIM image.

effect, the achievable resolution is dependent on the light fluence distribution on the focal plane. In deep imaging, the focal diameter deviates from the diffraction limit because of light scattering (Liu et al., 2012), a fact that also degrades the resolution of PIM. Consequently, in practice, the imaging depth of PIM is still restricted by the optical diffusion limit, which is ~1 mm in biological tissue.

For convenient operation, the data acquisition in the presented work was conducted in a frame-based manner. At each sampling pixel, the time interval between two consecutive excitation events is limited by the frame acquisition time, which can be relatively long owing to a large number of spatial sampling pixels. This limitation might compromise the PIM image formation in live cultures because phenomena such as fluorescence recovery after photobleaching (FRAP) can erase the memory of a sample on the previous light field distribution. To overcome this problem, the data acquisition of PIM can be switched to a point-based approach, measuring the entire fluorescence decay at a sampling pixel before the scanner moves to the next location. This method can minimize the time interval between two consecutive excitation events down to the integration time of the detector (200 μseconds in the presented study), a time scale within which the diffusion of fluorophores can be generally neglected.

MATERIALS AND METHODS

Numerical simulation for confocal and PIM fluorescence imaging

The numerical simulation for confocal and PIM fluorescence imaging was performed with Matlab (R2011a, MathWorks). Randomly distributed point objects were generated and are shown in Fig. 1D. The intensity of the laser scanning spot was considered to have a 2D Gaussian profile, yielding an illumination PSF in the form of

$$PSF_i = \exp[-\frac{(x-x_c)^2+(y-y_c)^2}{2\sigma^2}], \quad (9)$$

where (x_c,y_c) is the centroid of the laser spot, and σ is correlated to the FWHM of the PSF_i by FWHM=2.35σ.

The centroid of the laser spot was raster scanned across all pixels. After the first laser shot, the emitted fluorescence distribution at each sampling pixel (x_c,y_c) was calculated by

$$I_{f1}(x,y) = \mu_{a1}(x,y)[PSF_i(x,y)]^n, \quad (10)$$

where $\mu_{a1}(x,y)$ represents the initial absorption map, and n denotes the number of photons in an excitation event. For simplicity, the detection PSF was assumed to have the same distribution form as the illumination PSF in Eq. 9. The detected fluorescence intensity I^*_{f1} was thus equal to

$$I^*_{f1}(x_c,y_c) = \int I_{f1}(x,y)PSF_i(x,y)dxdy. \quad (11)$$

As a result of photobleaching, after the first laser shot the absorption coefficient map of the fluorophore became

$$\mu_{a2}(x,y) = \mu_{a1}(x,y)\exp\{-[PSF_i(x,y)]^m\tau\}. \quad (12)$$

Here τ is the pixel dwell time, and m denotes the order dependence of photobleaching on the laser fluence. Following a similar approach, the emitted and detected fluorescent intensities acquired after the second laser shot were derived as

$$I_{f2}(x,y) = \mu_{a2}(x,y)[PSF_i(x,y)]^n \text{ and} \quad (13)$$

$$I^*_{f2}(x_c,y_c) = \int I_{f2}(x,y)PSF_i(x,y)dxdy. \quad (14)$$

The signal intensity at position (x_c,y_c) in the conventional confocal image was given by

$$I_{CFM}(x_c,y_c) = (I^*_{f1}+I^*_{f2})/2. \quad (15)$$

In the corresponding PIM image, the signal intensity was given by

$$I_{diff}(x_c,y_c) = I^*_{f1}-I^*_{f2}. \quad (16)$$

To show the resolution improvement, we substituted previously reported values, m=5 and n=2, into the simulation for a fluorescence dye, aminocoumarin dextran, under two-photon excitation (Patterson and Piston, 2000). The resulting confocal fluorescence and PIM images are shown in Fig. 1D and Fig. 1E, respectively.

Fluorescence microscopy

The PIM experiments were implemented on a confocal laser-scanning microscope equipped with a multi-photon imaging unit (FV1000, Olympus). Two continuous-wave laser sources (Argon and He-Ne) provide a total of four wavelengths (405 nm, 488 nm, 543 nm and 632 nm) for one-photon excitation, and a Ti-sapphire femtosecond pulsed laser provides a tuneable wavelength (780–1060 nm) for two-photon excitation. The fluorescence was collected by a high NA microscope objective (PLAPON 60×O, NA=1.4, for one-photon excitation; 25× MPE water immersion, NA=1.05, for two-photon excitation) and was simultaneously detected by up to three separate PMT color channels. The laser excitation and acquisition of fluorescence images were controlled by the accompanying microscope software (Fluoview, Olympus).

Photobleaching imprinting microscopy (PIM)

PIM is achieved by monitoring photobleaching-induced fluorescence decay, followed by a pixel-by-pixel differential operation between two consecutive fluorescent images. The PIM procedure can be performed by using the time-lapse imaging module on a standard confocal microscope. To make surrounding regions unaffected at each sampling pixel, the scanning step size must be larger than the diffraction-limited PSF during acquiring a time-lapse dataset. Then we translate the sample a distance that is equal to half of the resolution of PIM and start the next cycle. The PIM images are calculated for each cycle and stitched together to form a final image.

Under the hypothesis that each fluorescence image captured along the time course is shot noise limited, the signal variance is correlated to the number of acquired photons N by the relation

$$\text{var}(I_f) = N. \quad (17)$$

The differential operation between I_{f1} and I_{f2} amplifies the variance by a factor of two, i.e.,

$$\text{var}(I_{diff}) = \text{var}(I_{f1})+\text{var}(I_{f2}) \approx 2\,\text{var}(I_{f1}) = 2N. \quad (18)$$

The SNR of the resulting differential image thus equals

$$SNR_{diff} = \frac{I_{f1}-I_{f2}}{\sqrt{\text{var}(I_{diff})}} \approx \frac{\Delta N}{\sqrt{2N}}, \quad (19)$$

where ΔN denotes the signal loss in photon count due to photobleaching.

To obtain a sufficient SNR to recover the features of the sample, in practice the differential intensity was averaged along the time course, yielding a final PIM image with an improved SNR

$$SNR_{PIM} \approx \sqrt{M}\,SNR_{diff}, \quad (20)$$

where M is the total number of acquired differential images. The focal drift compensation module of the microscope can be used to correct for the loss of focus caused by temperature changes around the microscope and other factors during time-lapse observation.

To extract high-order components from the PIM image, the time-lapse fluorescent decay at each pixel was fitted to a polynomial equation

$$I_f(t) = c_1+c_2t+c_3t^2, \quad (21)$$

where t is time, and c_1, c_2 and c_3 are the coefficients associated with F, F^2 and F^3 , respectively. The nonlinear components c_2 and c_3 provide the signal intensities in the corresponding PIM images, as shown in Fig. 3B,C.

Cell culture and fluorescent staining

NIH 3T3 fibroblast cells were cultured in Dulbecco's modified Eagle's medium supplemented with 10% fetal bovine serum, 2 mM glutamine, and 1% penicillin-streptomycin. The cells were incubated at 37℃ in 5% CO_2 and divided every ~72 hours. To prepare the cell slides, the fibroblast cells were seeded to a cover glass surface. The culture medium was removed 24 hours after seeding and replaced by the staining solution, 2 µM MitoTracker Orange probes (M-7510, Life Technologies) in fresh culture medium. After incubation in staining solution for 60 minutes, the cells were rinsed with fresh medium and then with phosphate buffered saline (PBS). The cell slides were then fixed in 4% formaldehyde for 15 minutes and then rinsed with PBS before imaging.

Acknowledgements

We thank J. Ballard for close reading of the manuscript. We would also like to thank L. D. Wang and J. Yao for helpful discussions.

Competing interests

L.W. has a financial interest in Microphotoacoustics, Inc. and Endra, Inc., which, however, did not support this work.

Author contributions

L.G. designed the biological experiment, performed part of the microscopy experiments, analyzed the data, and prepared the manuscript. A.G. analyzed part of data, and prepared the manuscript. Y.L. contributed to experimental design and performed part of microscopy experiments. C.L. prepared the biological sample and performed part of the microscopy experiments. L.V.W. contributed to the conceptual system and experimental design and manuscript preparation.

Funding

This work was sponsored in part by National Institutes of Health (NIH) [grant numbers DP1 EB016986 (NIH Director's Pioneer Award), R01 EB008085, R01 CA134539, U54 CA136398, R01 CA157277 and R01 CA159959]. Deposited in PMC for release after 12 months.

References

Betzig, E., Patterson, G. H., Sougrat, R., Lindwasser, O. W., Olenych, S., Bonifacino, J. S., Davidson, M. W., Lippincott-Schwartz, J. and Hess, H. F. (2006). Imaging intracellular fluorescent proteins at nanometer resolution. *Science* **313**, 1642-1645.

Burnette, D. T., Sengupta, P., Dai, Y. H., Lippincott-Schwartz, J. and Kachar, B. (2011). Bleaching/blinking assisted localization microscopy for superresolution imaging using standard fluorescent molecules. *Proc. Natl. Acad. Sci. USA* **108**, 21081-21086.

Fahrbach, F. O., Gurchenkov, V., Alessandri, K., Nassoy, P. and Rohrbach, A. (2013). Self-reconstructing sectioned Bessel beams offer submicron optical sectioning for large fields of view in light-sheet microscopy. *Opt. Express* **21**, 11425-11440.

Gustafsson, M. G. L. (2000). Surpassing the lateral resolution limit by a factor of two using structured illumination microscopy. *J. Microsc.* **198**, 82-87.

Gustafsson, M. G. L. (2005). Nonlinear structured-illumination microscopy: wide-field fluorescence imaging with theoretically unlimited resolution. *Proc. Natl. Acad. Sci. USA* **102**, 13081-13086.

Hell, S. W. (2007). Far-field optical nanoscopy. *Science* **316**, 1153-1158.

Helmchen, F. and Denk, W. (2005). Deep tissue two-photon microscopy. *Nat. Methods* **2**, 932-940.

Hess, S. T., Girirajan, T. P. K. and Mason, M. D. (2006). Ultra-high resolution imaging by fluorescence photoactivation localization microscopy. *Biophys. J.* **91**, 4258-4272.

Klar, T. A., Jakobs, S., Dyba, M., Egner, A. and Hell, S. W. (2000). Fluorescence microscopy with diffraction resolution barrier broken by stimulated emission. *Proc. Natl. Acad. Sci. USA* **97**, 8206-8210.

Lichtman, J. W. and Conchello, J. A. (2005). Fluorescence microscopy. *Nat. Methods* **2**, 910-919.

Liu, Y., Zhang, C. and Wang, L. V. (2012). Effects of light scattering on optical-resolution photoacoustic microscopy. *J. Biomed. Opt.* **17**, 126014-126014.

Munck, S., Miskiewicz, K., Sannerud, R., Menchon, S. A., Jose, L., Heintzmann, R., Verstreken, P. and Annaert, W. (2012). Sub-diffraction imaging on standard microscopes through photobleaching microscopy with non-linear processing. *J. Cell Sci.* **125**, 2257-2266.

Murray, J. M. (2011). Methods for imaging thick specimens: confocal microscopy, deconvolution, and structured illumination. *Cold Spring Harb. Protoc.* **2011**, pdb.top066936.

Patterson, G. H. and Piston, D. W. (2000). Photobleaching in two-photon excitation microscopy. *Biophys. J.* **78**, 2159-2162.

Piston, D. W. (1999). Imaging living cells and tissues by two-photon excitation microscopy. *Trends Cell Biol.* **9**, 66-69.

Rust, M. J., Bates, M. and Zhuang, X. W. (2006). Sub-diffraction-limit imaging by stochastic optical reconstruction microscopy (STORM). *Nat. Methods* **3**, 793-795.

Simonson, P. D., Rothenberg, E. and Selvin, P. R. (2011). Single-molecule-based super-resolution images in the presence of multiple fluorophores. *Nano Lett.* **11**, 5090-5096.

Theer, P. and Denk, W. (2006). On the fundamental imaging-depth limit in two-photon microscopy. *J. Opt. Soc. Am. A Opt. Image Sci. Vis.* **23**, 3139-3149.

Tsien, R. Y., Ernst, L. and Waggoner, A. (2006). Fluorophores for confocal microscopy: Photophysics and photochemistry. In *Handbook of Biological Confocal Microscopy* (ed. J. B. Pawley), pp. 338-352. New York, NY: Springer.